AMERICAN SOCIETY FOR MICROBIOLOGY | Applied and Environmental Microbiology

Nanomechanical Characterization of *Bacillus anthracis* Spores by Atomic Force Microscopy

Alex G. Li,[a] Larry W. Burggraf,[a] Yun Xing[b]

Department of Engineering Physics, Air Force Institute of Technology, Wright-Patterson Air Force Base, Ohio, USA[a]; Oak Ridge Institute for Science and Education (ORISE), Oak Ridge, Tennessee, USA[b]

ABSTRACT

The study of structures and properties of bacterial spores is important to understanding spore formation and biological responses to environmental stresses. While significant progress has been made over the years in elucidating the multilayer architecture of spores, the mechanical properties of the spore interior are not known. Here, we present a thermal atomic force microscopy (AFM) study of the nanomechanical properties of internal structures of *Bacillus anthracis* spores. We developed a nanosurgical sectioning method in which a stiff diamond AFM tip was used to cut an individual spore, exposing its internal structure, and a soft AFM tip was used to image and characterize the spore interior on the nanometer scale. We observed that the elastic modulus and adhesion force, including their thermal responses at elevated temperatures, varied significantly in different regions of the spore section. Our AFM images indicated that the peptidoglycan (PG) cortex of *Bacillus anthracis* spores consisted of rod-like nanometer-sized structures that are oriented in the direction perpendicular to the spore surface. Our findings may shed light on the spore architecture and properties.

IMPORTANCE

A nanosurgical AFM method was developed that can be used to probe the structure and properties of the spore interior. The previously unknown ultrastructure of the PG cortex of *Bacillus anthracis* spores was observed to consist of nanometer-sized rod-like structures that are oriented in the direction perpendicular to the spore surface. The variations in the nanomechanical properties of the spore section were largely correlated with its chemical composition. Different components of the spore materials showed different thermal responses at elevated temperatures.

Structures and material properties of bacterial spores play an important role in protecting them against a variety of environmental stresses, such as toxic chemicals (1), radiation (2, 3), and heat (3–5). The current knowledge of spore structures has been obtained largely using transmission electron microscopy (TEM) methods in various forms (6–20). A mature spore usually shows a concentric multilayer structure, consisting of the core, inner membrane, germ cell wall, cortex, outer membrane, and coat assembly. For *Bacillus anthracis* spores, there is an exosporium layer that loosely encases the spore. The spore core, which contains mostly DNA, RNA, enzymes, and dipicolinic acid (DPA), is in a dehydrated and metabolically dormant state (21–25). The ability of bacterial spores to survive for long durations, sometimes in harsh environments, has been attributed to the immobilization of essential DNA, RNA, and enzymes by small, acid-soluble spore proteins (SASP) (28–30). It was suggested that the DPA can be intercalated with spore DNA and RNA through covalent bonds, forming a gel-like polymer matrix (26, 27). It is worth mentioning that the DPA structure in the spore core is not well understood. The germ cell wall (e.g., inner cortex) and outer cortex of spores are two integrated peptidoglycan (PG) structures (31–41). The germ cell wall is similar to the vegetative cell wall, consisting of glycan chains of alternating *N*-acetylglucosamine (NAG) and *N*-acetylmuramic acid (NAM) residues. A peptidoglycan network is formed through cross-linking between peptide side chains on the NAM residues. The cortex peptidoglycan is characterized by a low degree of peptide cross-linking, resulting from peptide side chain removal and muramic acid conversion to muramic lactam. The loosely cross-linked PG cortex has been hypothesized to play a role in protoplast dehydration (31). During spore germination, the cortex is rapidly degraded by peptidoglycan lytic enzymes. The germinated spore loses its outer cortex and coat, and its inner spore cortex becomes the cell wall of the vegetative cell. It is worth mentioning that the loosely cross-linked peptidoglycan can exhibit a significant change in volume when the spore is exposed to different ionic environments or humidity. The bonding between the loosely cross-linked PG and other spore materials, such as the coat and germ cell wall, may be weak because the cortex materials can be dissolved and washed away in the thin sections of formalin-fixed *Bacillus megaterium* spores (32). Thwaites et al. (33) suggested that the PG can add mechanical strength to the cell envelope and maintains cell shape. However, Popham et al. (37) argued that the cortex role in spore dehydration is not mechanical in nature, rather serving as a static structure to maintain dehydration. Even though the structure of the bacterial peptidoglycan has been extensively studied for decades, it is still debatable how the

Received 9 February 2016 **Accepted** 4 March 2016

Accepted manuscript posted online 11 March 2016

Citation Li AG, Burggraf LW, Xing Y. 2016. Nanomechanical characterization of *Bacillus anthracis* spores by atomic force microscopy. Appl Environ Microbiol 82:2988–2999. doi:10.1128/AEM.00431-16.

Editor: D. W. Schaffner, Rutgers, The State University of New Jersey

Address correspondence to Alex G. Li, Alex.Li@afit.edu.

Supplemental material for this article may be found at http://dx.doi.org/10.1128/AEM.00431-16.

PG strands are arranged in the cell wall and spore cortex. Many believed that the peptidoglycan strands form regular planar networks parallel to the plasma membrane. However, there were several studies that suggested that the peptidoglycan strands are oriented perpendicular to the plasma membrane (39–41). In addition, the length distribution and elasticity of the PG strands are not known. TEM studies of Gan et al. (19) showed that the PG strands were circumferential, parallel to the cell membrane, and perpendicular to the long axis of the cell. More recently, the electron cryotomography study of Tocheva et al. (15) showed that vegetative *Bacillus subtilis* cells and mature spores both are surrounded by a thick layer of peptidoglycan, revealing the presence of a PG-like layer throughout engulfment. Two thick layers of cortex were apparent between the inner and outer spore membranes. The inner cortex (e.g., the germ cell wall) was denser and more uniform in thickness (50 to 70 nm) than the outer cortex (50 to 100 nm). They suggested that both forms of the PG materials have the same circumferential architecture. However, the nuclear magnetic resonance (NMR) studies of Dmitriev et al. (39) suggested a scaffold model in which the PG strands in a normal orientation to the cell surface. Computer simulation by Dmitriev et al. (40) indicated that a moderate degree of the PG cross-linking makes a planar peptidoglycan unfavorable. The AFM studies of Hayhurst et al. (41) indicated that the PG strands of *B. subtilis* sacculi were bundled together, forming hollow cables around the cells.

The spore coat usually is composed of a multilayer structure of highly cross-linked proteins (42–44). The number of the proteinaceous layers varies from species to species. In addition to predominant proteins, the coat also contains small amounts of carbohydrates and lipids. The primary function of the coat is known to provide mechanical and chemical protection for the spore. The coat can limit harmful chemicals from entering the spore interior while allowing small-molecule nutrients and germinants to pass through. The coat can contract and expand in response to changes in the environment and biological processes, e.g., germination. For example, dormant spores of *Bacillus thuringiensis* expand and shrink in response to increasing and decreasing relative humidity on different time scales from tens of seconds to minutes (45). The contraction of the coat often is accompanied by the formation of small ridges on the spore surface (46). Plomp et al. (47–50) showed that the surface of *Bacillus thuringiensis* is covered with crystalline hexagonal honeycomb structures; the surface of *Bacillus cereus* spores is covered with small randomly oriented domains. The AFM studies of Chada et al. (51), Giorno et al. (52), and Wang et al. (53) revealed that the *Bacillus* spore surface is covered with nanometer-sized circular bumps. The surface of *Bacillus subtilis* and *Bacillus anthracis* spores is populated by ridge structures largely oriented with the long axis of the spore. We previously showed that four closely related species of *Bacillus* spores can be distinguished by surface morphology analysis (54). Using thermal atomic force microscopy (AFM), we recently characterized thermal effects on the topographic morphology and nanomechanical properties of *Bacillus anthracis* spores at elevated temperatures (55, 56). We observed striking changes resembling phase transitions in the physical properties of heated spores on the nanometer scale. It is not clear how the coat is designed to achieve high stiffness while maintaining large elastic flexibility. However, even less is known about the physical properties of the spore, particularly the spore interior.

Leuschner and Lillford (14) investigated the molecular mobility of ^{31}P and ^{13}C in dormant *Bacillus subtilis* spores with different water concentrations using high-resolution solid-state NMR. The molecular mobility in the freeze-dried spores generally was low but increased significantly with increasing water content in the spores. The ^{13}C mobility in the dipicolinic acid was independent of hydration, while the ^{31}P mobility in the core was strongly dependent on hydration, which suggests that the DPA is immobilized in the spore core. The NMR analysis of Bradbury et al. (57) indicated that the mobility and concentration of water in the core are higher than those in the coat and cortex. Ghosal et al. (58) studied water and ion uptake into the core of dormant *Bacillus thuringiensis* spores. Using isotopic and elemental gradients in the *B. thuringiensis* spores, they showed that deuterated water (D_2O) and solvated ions can permeate throughout and be incorporated into the whole spore.

In this work, we describe an AFM method for producing spore sections and characterizing the internal structure and nanomechanical properties at elevated temperatures. Our AFM method is composed of a two-step procedure. First, we fracture the spore by means of indentation using a stiff diamond AFM tip to expose the interior of dormant spores. Second, we image the surface morphology and probe the nanomechanical properties of the fractured spore using a soft, sharp AFM tip. We were able to study the spore section for the first time using a non-TEM method. We observed a previously unknown ultrastructure of the spore interior. We showed that there were significant changes in the structures and properties of the spore section. Different spore components exhibited different thermal responses. Our findings may advance the understanding of the architecture and properties of spores.

MATERIALS AND METHODS

Sample preparation. *Bacillus anthracis* spores (Sterne strain, Thraxol-2, code 235-23) were grown on nutrient agar at 35°C for about 7 days. The spores were transferred to a microcentrifuge tube and washed at least three times with sterile deionized water after they were harvested from the agar plates using a sterile cell scraper. The spore purity was confirmed to be greater than 95% by microscopic examination. The spores were incubated on a heating block at 65°C for 30 min to inactivate vegetative growth and washed again with DI water before storage at 4°C or measurement at room temperature. For AFM imaging of individual spores, a drop of 10 μl diluted spore suspension containing about 10^5 spores was placed on freshly cleaved mica. The spores were air dried in a biosafety level 2 cabinet for at least 12 h before they were characterized using the atomic force microscope.

Nanosurgical AFM method. The AFM method we used for studying internal structures and properties of spores was a two-step procedure. First, a stiff diamond AFM tip was used to cut the spore by indentation, exposing the cross-sectional surface. Second, a sharp silicon or silicon nitride AFM tip was used to characterize the newly fractured spore section, as illustrated in Fig. 1a and b. We explored two different cutting techniques, which are referred to here as the point-cut and the line-cut methods. In a typical point-cut operation, the diamond tip was placed at a selected location on the spore surface, followed by one or multiple indentations until the indenter completely cut through the spore. The triangular indentation mark produced by the diamond cube-corner tip was characteristic of the point-cut procedure, as shown in Fig. S1 in the supplemental material. Similarly, the line-cut procedure involved cutting the spores at a series of evenly and closely spaced locations on the sample surface, producing a fracture line across several spores, as shown in Fig. S2. In order to distinguish between the native and freshly cut spore sur-

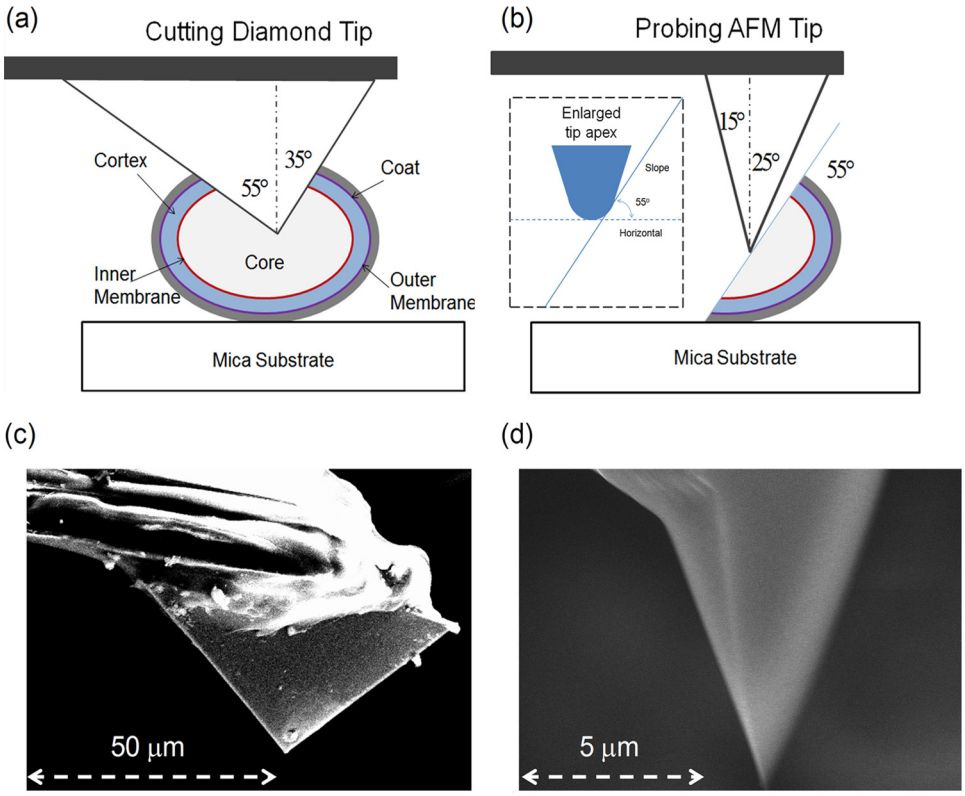

FIG 1 Schematic diagrams of the nanosurgical AFM method for producing a cross-sectional sample surface of a single spore using a stiff diamond AFM tip (a) and characterizing the surface structure and properties of the spore section using a sharp silicon AFM tip (b). Representative SEM images (side view) of the cube-corner diamond AFM tip (c) and the silicon AFM tip (d) are shown. The major structural components (not drawn to scale) of the *Bacillus* spores from center to outer surface are the spore core, inner membrane, cortex, outer membrane, and spore coat.

face, we generated prior to cutting identifiable surface marks by scratching the spore surface with the diamond tip, as shown in Fig. 2d to f. When the surface of spores was scanned by the stiff diamond AFM tip, the spores lost the original ridge structures that are frequently observed on dehydrated spores (Fig. 2b, arrows), showing nanometer zig-zag patterns (Fig. 2e, arrows). The tip-induced reconstructions in the surface of the spore coat can be explained in terms of the mechanical instability of a bilayer thin film under shear stress (59). The presence of the distinct surface marks made it easy for us to distinguish the newly created section from the coat surface of the spore. Other surface features, e.g., large clusters of spores, dust, or substrate defects, also were useful for quick searching and locating the target spores. The load required to cut through a spore varied from tens of nanonewtons to micronewtons depending upon the stiffness of the spore. When a small load was applied, multiple indentations usually were required. The depth of tip indentation was monitored by the force curves. When the diamond tip cut through the spore, the slope of the loading force curve, which is proportional to the stiffness of the sample surface, increased quickly as the tip approached the stiff substrate. Since the AFM sectioning procedures were intensively time-consuming, it was difficult to sample a large number of spores. However, to ensure that the selected target spores were representative of the statistical ensemble, we randomly selected each sample from the mica substrate, which was populated by approximately 200 to 1,000 spores, depending upon the coverage. The stiff indenter we used here was a calibrated diamond cube corner tip with a spring constant of 186 N/m. The following nominal specifications of the diamond AFM tip were used: tip height, 50 μm; front angle (FA), 55°; back angle (BA), 35°; side angle (SA), 45°; average tip radius, 40 nm; cantilever length, 350 μm. A representative scanning electron microscope image of the diamond tip is shown in Fig. 1c. It should be pointed out that the spore section produced by this method is oriented at an angle to the substrate plane, largely depending upon the geometry of the indenter. For a cube-corner diamond tip, the inclination angle falls between 45° and 55°, varying with the deflection angle of the cantilever beam.

Figure 3 shows representative AFM images of a freshly cut spore section (referred to here as sample no. 1), located at the lower end of the spore cluster, together with four other intact spores (no. 2 to 5). The intact spores were easily recognizable by their size, shape, and surface morphology. The external coat surface of the spore was populated with the tip-induced surface marks. The triangular indentation print on the spore, which is characteristic of the cube corner diamond tip (Fig. 3a, white arrow), provided us with additional topographic features for identifying the spore section. We observed that most of the fractured spore sections were associated with the front surface of the diamond tip. Additional AFM images of the spore sections can be found in the supplemental material (e.g., see Fig. S3 and S4).

Nanomechanical measurement. The AFM instrument we used to characterize the surface structures and properties of spores was a NanoScope multimode atomic force microscope with peak force imaging capability from Bruker Corporation. For nanomechanical measurement, the atomic force microscope was operated in intermittent contact mode. The cantilever tip was oscillated at low amplitude (10 to 100 nm) and low modulation frequency (0.5 to 2 kHz). The load applied to the AFM tip was maintained as a small preset value (0.3 to 50 nN). The piezoelectric scanner (AS-130VLR) of the AFM instrument is capable of imaging 125 μm by 125 μm in the lateral *x* and *y* axis directions and 5 μm in the vertical *z* axis direction. Surface properties such as modulus, adhesion, deformation, and dissipation were measured simultaneously and processed using the commercial Multimode 8 NanoScope analysis software.

The Young's modulus of the sample was obtained by fitting the un-

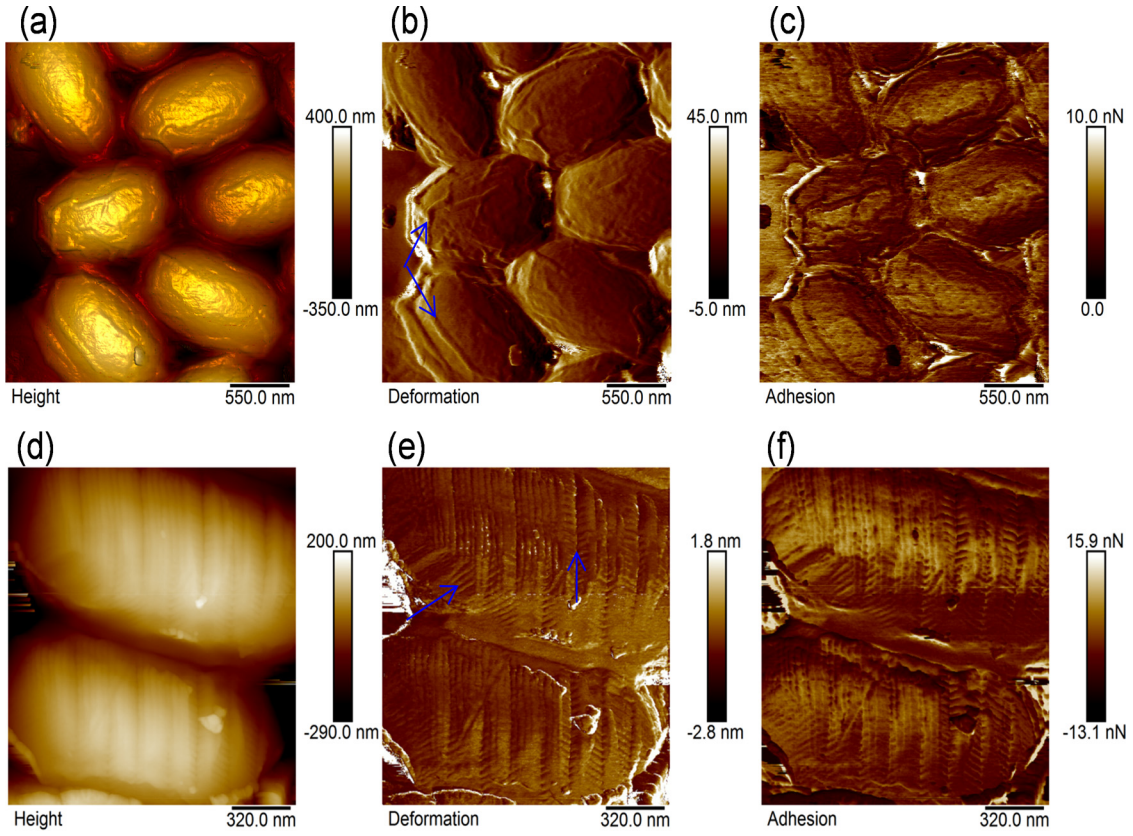

FIG 2 AFM images of the *Bacillus anthracis* spore surfaces without (a to c) and with (d to f) the tip-induced surface marks on the mica substrate. The top row includes the height (a), deformation (b), and adhesion (c) image of the intact, native surface of the spores. The bottom row includes the height (d), deformation (e), and adhesion (f) image of the patterned surface of the spores. The images are plane-fitted using the line-by-line algorithm and rescaled for visual clarity.

loading portion of the force-distance curve using the Derjaguin-Muller-Toporov (DMT) model (60), as given by

$$F - F_{\text{adhesion}} = \frac{4}{3}E^{*}\sqrt{R(d - d_0)^3}$$

where F is the load, F_{adhesion} is the adhesion force, E^{*} is the reduced modulus, R is the radius of the tip, and $(d - d_0)$ is the deformation in the surface. The reduced modulus is defined by $E^{*} = [(1 - \nu_s^2)/E_s + (1 - \nu_{\text{tip}}^2)/E_{\text{tip}}]^{-1}$, where ν is the Poisson's ratio and E is the Young's modulus of the tip and sample (s), respectively, as indicated by the subscripts. It should be emphasized that for viscoelastic materials such as spore polymers, the modulus measured at a high frequency (e.g., 2 kHz) can be significantly larger than that obtained using the static measurement (e.g., nanoindentation) or at a near-zero frequency. In addition, since the nominal radius of the cantilever tip was used in this work, the measured elastic modulus was qualitative. Unless specified, the AFM modulus images shown in this work were the raw or uncorrected data. The deformation image displayed approximately 85% of the maximum distance at which the tip penetrates into the surface at a load equal to the peak force. Therefore, the deformation can be viewed as an indirect measure of the stiffness of the sample surface, which provides information similar to that of the modulus in most cases, except for situations when the adhesion force is dominant. The adhesion force was determined from the pull-off position in the force-distance curve on each point of contact. The adhesion force can be produced by any attractive force, such as van der Waals, electrostatics, and capillary meniscus of thin liquid film on the sample surface. For silicon-based cantilever tips, the tip surface usually is covered with hydroxyl groups due to surface reactions with water in air. The adhesion force between the hydrophilic tip and sample surface likely is dominated by hydrogen bonds in water and other polar molecules of the spore surface.

It should be pointed out that for an inclined surface the modulus image often is convoluted with the slope (e.g., peak force image) of the sample surface, as shown in Fig. S5 in the supplemental material. In order to properly characterize the modulus of the spore section (e.g., core and cortex), we utilized a relative comparison method in which the modulus was evaluated along equal contour lines of the peak force image. To do this, the peak force image was overlaid with the property image (e.g., modulus or adhesion). The intensity of each composite RGB image was rescaled independently and displayed in different color bands using commercial code (e.g., Matlab). The gray regions in the composite image showed where the two images have the same intensities, implying that the peak force and the property images were positively correlated. The magenta regions showed where the property intensities were relatively larger, while the green regions showed where the peak force intensities were relatively larger (e.g., two images are negatively or not correlated), as shown in Fig. S6. The slope effect sometimes can be reduced by rotating the sample or the direction of the tip scan to minimize changes in peak force.

Surface heating at nanometer contact. The localized heating at the nanometer contact of the spore surface was achieved by scanning a heated AFM tip (AN2-200) in intermittent contact with the surface. Our AFM system was equipped with the nano-TA controller for thermal AFM tips from Anasys Instruments. The temperature of the thermal tip was controlled through joule heating in a U-shaped resistor formed in the silicon

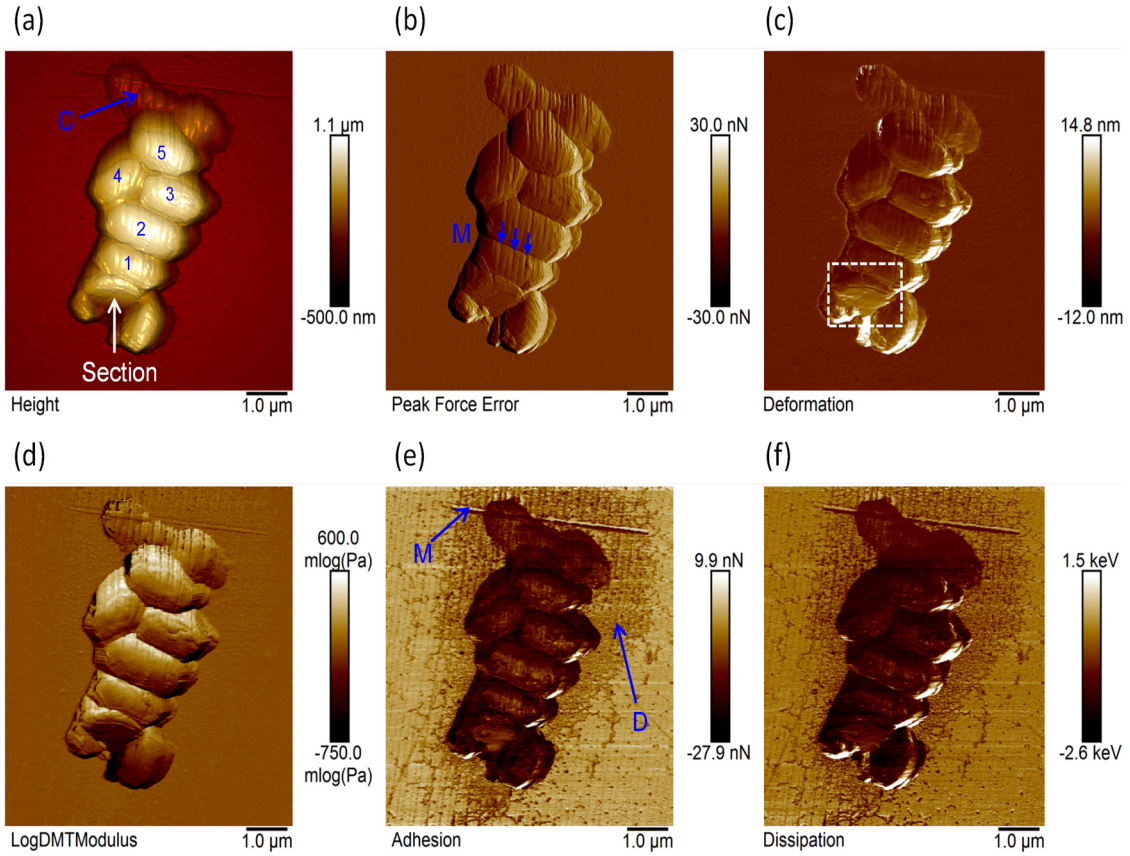

FIG 3 AFM images of a cluster of spores with the tip-induced marks on the coat surface. (a) Height with the lighting illumination effect; (b) peak force; (c) deformation; (d) modulus on the logarithmic scale; (e) adhesion; (f) dissipation. The following AFM parameters were used: scan size, 7.2 μm; scan rate, 1 Hz; number of samples/line, 512; line direction, retrace; capture direction, down; scan angle, 90°; control gain, 18; amplitude set point, 33 nN; drive amplitude, 120 nm at 2 kHz; spring constant, 2.5 N/m; tip radius, 30 nm. The AFM images were line fitted using the line-by-line algorithm, flattened, and rescaled for visual clarity. The incident light was in the positive *y* axis direction and at 25° off the *x*-*y* plane. The cutting diamond tip was aligned in the positive *y*-axis direction (arrow in panel a).

cantilever beam by a doping process. For constant-temperature AFM measurement, the AFM tip was quickly heated to the preset temperature at a rate of about 1,000°C/s. The heating time (or dwell time) at the tip-surface contact is very short, about 5×10^{-4} s, at a modulation frequency of 2 kHz. Our finite element analysis modeling substantiated that the temperature distribution in the spore supported by a silicon substrate can reach its steady state within a time of less than 5×10^{-4} s (55). The spring constant of the thermal tip, ranging from 0.5 to 3 N/m, was determined using the thermal tune method (61). The detailed specifications for the thermal cantilever tip are the following: tip height, 3 to 6 μm; tip radius, <30 nm; cantilever length, thickness, and resonant frequency, 200 μm, 2 μm, and 55 to 80 kHz, respectively. We assume that the FA, BA, and SA of the thermal silicon tip are close to those of common pyramid silicon tips, which are about 25°, 15°, and 22.5°, respectively. The SEM image (Fig. 1d) shows a representative side view of the silicon tip. All AFM tips were rinsed with high-purity methanol and acetone before use. In addition, the thermal tip was briefly heated to about 400°C for 10 s to remove possible contaminations before each measurement. For thermal tip temperature calibration, the AFM was operated in contact mode on the vendor calibration samples. The temperature calibration curve was produced by quadratic fitting of the melting points (T_m) of polyethylene terephthalate (PET; T_m = 235°C), high-density polyethylene (HDPE; T_m = 116°C), and polycaprolactone (PCL; T_m = 55°C) to the corresponding heating voltages at which the crystalline polymers start to melt, similar to our previous calibration (62).

RESULTS AND DISCUSSION

Nanostructures of the spore section. High-resolution AFM images of the spore section (no. 1; enclosed area in Fig. 3c) are shown in Fig. 4. The structural components of the spore section, including the core, cortex, and coat, were identified based upon current knowledge about the spore architecture (6–20). It has been well documented that the core is located at the center of the ellipsoid-shaped spore of about 1 to 2 μm in size. Therefore, we assigned the central region of the section to be the core area of the spore (enclosed by the white dashed line 1 in Fig. 4a). The upper right region was assigned to be the coat of the spore because of the presence of the surface marks (e.g., zig-zag patterns) we created on the native coat layer of the spore samples (Fig. 2 and 3). The narrow region between the core and coat must belong to the cortex of the spore. The boundary between the coat and cortex, where the outer membrane is expected to be located, appeared to be sharp and well defined (blue line 2 in Fig. 4a). A small segment of the coat may have been torn off the cortex (solid line 3 in Fig. 4a), suggesting a weak coat-cortex interface. The thickness of the cortex layer varied from 90 to 150 nm, consistent with the dimensions observed in most TEM studies (8–10). The thinnest cortex was near the polar region of the long axis; the thickest cortex was near the short

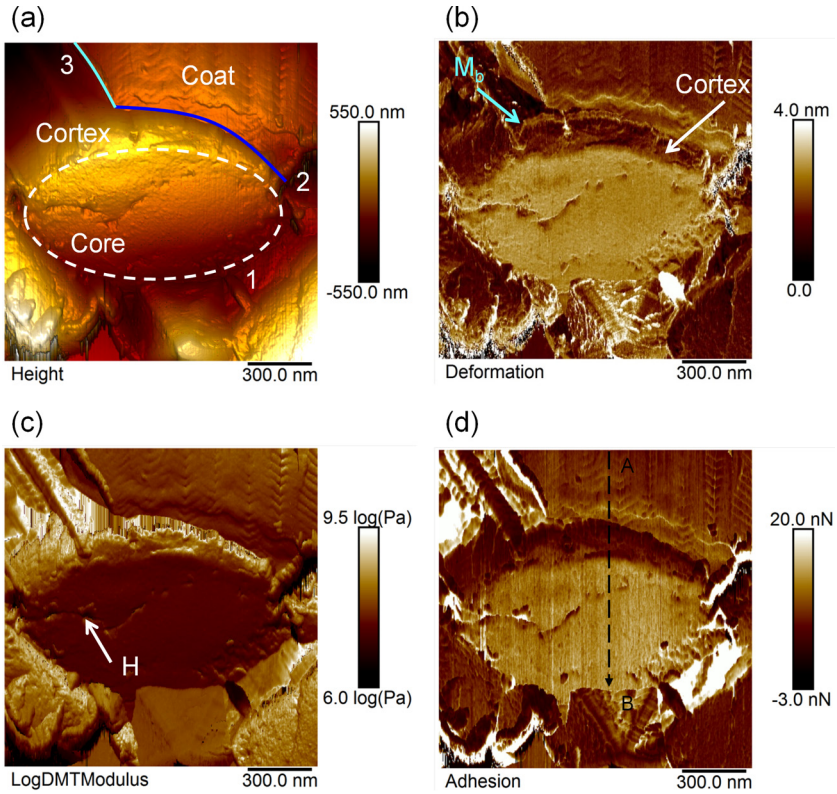

FIG 4 AFM images of the cross-section of a fractured dormant spore, as displayed in Fig. 3, at ambient temperature in air. (a) The height image is a rescaled three-dimensional presentation of the AFM image. The core area of the spore is enclosed by white dotted line 1. The boundary between the coat and cortex is indicated by solid line 2. (b) To show deformation, the cortex layer is indicated by the white arrow; the membrane-like structure is highlighted by the arrow labeled M_b. (c) Raw modulus image on the logarithmic scale. The surface defects are indicated by arrow H. (d) Adhesion. The images are plane fitted using the line-by-line algorithm and rescaled for visual clarity. The lighting effects are used to enhance the visual depth of the height images, namely, incident light in the positive *y* axis direction and at 25° off the *x*-*y* plane. The following AFM parameters were used: scan size, 1.5 μm; scan rate, 1 Hz; number of samples/line, 512; line direction, retrace; capture direction, down; scan angle, 90°; control gain, 9; amplitude set point, 3.0 nN; drive amplitude, 120 nm at 2 kHz; spring constant, 2.5 N/m; tip radius, 30 nm.

axis. However, it is not clear whether or not our AFM observations of the cortex thickness distribution can be generalized to the whole spore population. A thin membrane-like structure of about 10 nm in thickness was apparent at the interface between the coat and cortex (M_b in Fig. 4b and the blue line in Fig. 6 and 7). It is worth mentioning that it is still debatable whether or not mature *Bacillus* spores have an outer membrane or a complete membrane (16).

The surface morphology of the spore core appeared to be relatively smooth and uniform compared to those of other surrounding spore materials except for a few small cracks and holes (Fig. 4 and 5). The nature of these defects, which may be intrinsic or produced by the fracture force during tip indentation, is not known. The mechanical properties of the spore core, such as deformation, modulus, and adhesion, also followed a similar tread without significant variations over the majority of the core area (Fig. 4b to d). However, when imaged at a higher resolution (Fig. 5), the core was shown to be comprised of small, dense granular particles of a mean diameter of about 10 nm. The deviation in the diameter, which was measured by the difference between 5% and 95% of the histogram values, was about 18 nm. The similar granular structures, which were observed by the TEM study of Tocheva et al. (16) to be distributed throughout the cytoplasm, were attributed to cell ribosomes and proteins embedded in the DPA.

The cortex of the spore was characterized by the loosely packed nanoparticles that were larger than the granular particles in the core (Fig. 4b). High-resolution images of the spore section showed that the cortex appeared to be composed of a two-layer structure; the boundary between these two cortex layers is highlighted by the green lines in Fig. 6b to d. The outer layer of the cortex appeared to be composed of rod structures that were oriented perpendicular to the spore surface. These rods were about 10 nm in width and 60 nm in length. The inner layer of the cortex, which can be designated the germ cell wall, was comprised mainly of small, loosely packed particles of about 10 nm in width and 20 nm in length. We have confirmed that the rod orientation was not dependent upon the direction of the AFM tip scan. When the direction of the tip scan was changed by 90°, the orientation of the cortex strand showed no change. Since the width of these rods was significantly larger that the diameter of individual glycan strands, these rods could be bundle or coil structures of the PG strands. We observed that these loosely packed cortex particles in the germ cell wall occasionally could be displaced or removed by a scanning AFM tip, indicating that the interactions between these particles are not strong. Our observation is consistent with the current understanding of the cortex materials, which are made mainly of the low-cross-linking peptidoglycan polymer (31–41) and can be dissolved and washed away in the thin sections of formalin-fixed *B. megaterium* spores (38). While it is possible that the formation of

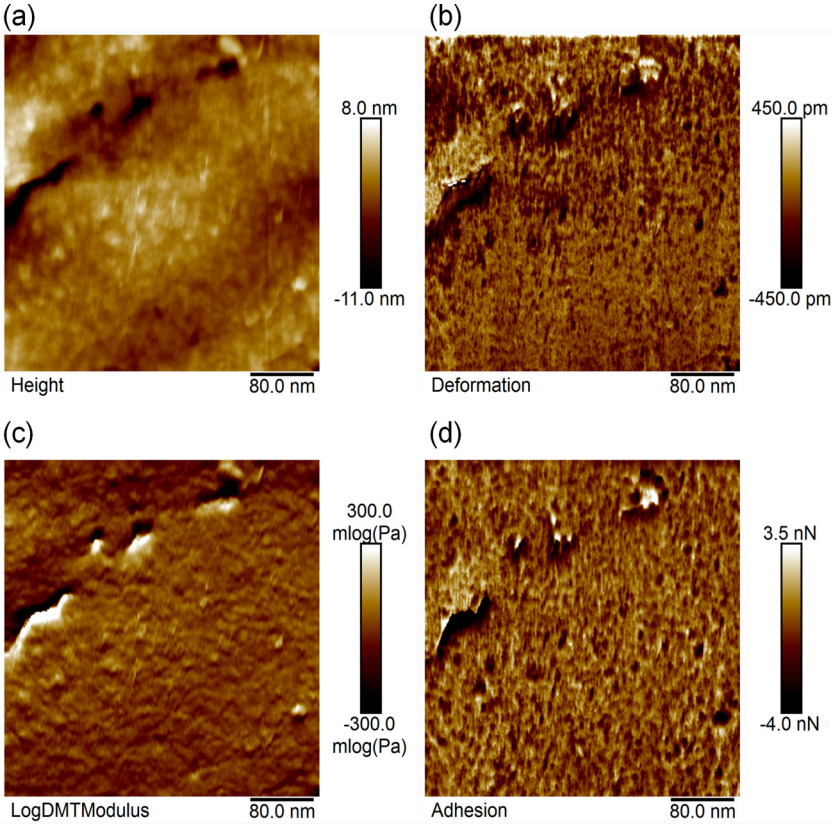

FIG 5 High-resolution AFM images of the core of the spore at ambient temperature in air on the mica substrate. (a) Height. (b) Deformation. (c) Raw modulus image on the logarithmic scale. (d) Adhesion. All of the AFM images were rescaled for a clear view. In addition to the rescaling, the height image also was flattened. Mean particle diameter in panel a, 10 nm. Deviation, 18 nm (the difference between 5% and 95% histograms). The images are plane fitted using the line-by-line algorithm and rescaled for visual clarity. The following AFM parameters were used: scan size, 1.5 μm; scan rate, 1 Hz; number of samples/line, 512; line direction, retrace; capture direction, down; scan angle, 90°; control gain, 6; amplitude set point, 1.1 nN; drive amplitude, 120 nm at 2 kHz; spring constant, 2.5 N/m; tip radius, 30 nm.

the rod-like structures in the cortex are related to the spatial arrangement of the muramic-lactam residues and/or the cross-linked peptide side chains parallel with the surface plane of the spore, such a picture is unlikely in our case, because the strong peptide cross-linking interactions between PG strands are likely to form a cohesive polymer shell instead of a loose granular layer, as observed by us and others (38). With the AFM resolution achieved, it is not clear how rod orientation is correlated with strand orientation. We anticipate being able to measure the ultrastructure of the spore cortex at higher resolution in the future. The interface between the core and cortex, where the inner membrane is expected to be located, showed significant discontinuities (Fig. 6b to d). Some segments of the interface (indicated by the solid lines) appeared to be sharp and well defined; others (indicated by the dotted lines) appeared to be diffuse and not well defined. Our findings suggested that the inner membrane in the spore is damaged by the fracture force during sample preparation. The ultrastructure of the cortex became more apparent when the AFM images were inverted, as shown in Fig. 7. The changes in surface morphology and properties (e.g., stiffness and adhesion) are significantly different for the core, cortex, and coat regions. Additional AFM images of the spore sections can be found in the supplemental material. We have produced and examined more than a dozen spore sections. It should be pointed out that while the overall sectional structures of the different spore samples we studied in this work were similar to each other, the ultrafine structures of each primary spore component, such as the core and cortex, varied slightly from sample to sample, as shown in the supplemental material. The variations were mostly in the cortex layer of the spores, because the cortex material showed loose granular properties.

Nanomechanical properties of the spore section. Using the equal-contour analysis method we describe in the supplemental material, we showed significant changes of the nanomechanical properties in the core, cortex, and coat of the spore, as shown in Fig. 8. As the AFM tip scanned from the coat (right end) to the core regions (Fig. 4d, fast scan in the *x* axis direction and slow scan in the *y* axis along line AB), the peak force curve exhibited small fluctuations across the different regions, except for a jump in the outer cortex layer (indicated by the arrow). Because the slope effect is negligible when the variations of the peak force along the direction of fast scan are small, we can directly compare the material properties of the spore section using the raw AFM images without correcting the slope effect. The elastic modulus (Y) of the spore section decreased in the following order: $Y_{\mathrm{cortex}} > Y_{\mathrm{coat}} > Y_{\mathrm{core}}$. The adhesion force ($F$) of the spore decreased in the following order: $F_{\mathrm{core}} > F_{\mathrm{coat}} > F_{\mathrm{cortex}}$. The deformation ($D$) of the spore decreased in the following order: $D_{\mathrm{core}} > D_{\mathrm{coat}} > D_{\mathrm{cortex}}$. The

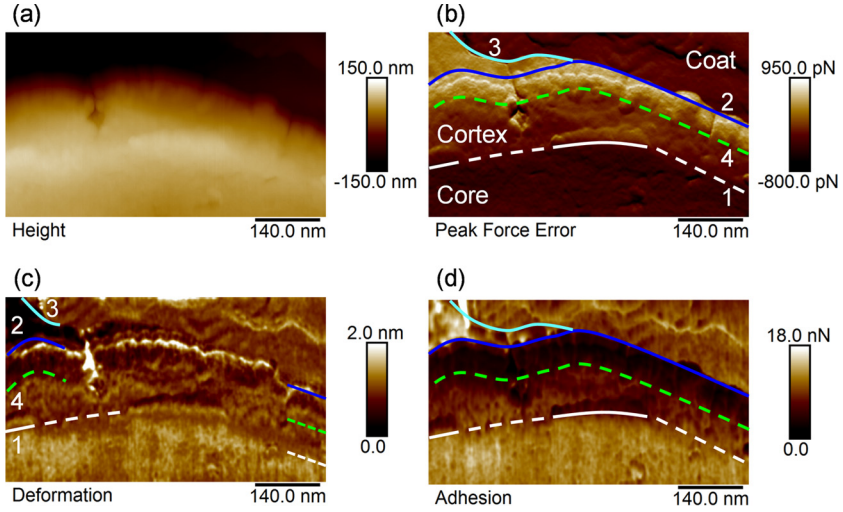

FIG 6 High-resolution AFM images of the multilayer structure of the core, cortex, and coat of the spore at ambient temperature in air. (a) Height (rescaled). (b) Peak force. (c) Deformation. (d) Adhesion. The interface between the core and cortex is indicated by line 1. The well-defined boundaries are highlighted by the solid line, while the less well-defined boundaries are highlighted by the dotted lines. The interface between the cortex and coat is indicated by line 2. The boundary between the torn-off coat and air is labeled by line 3. The possible interface between two cortex layers is suggested by line 4. The following AFM parameters were used: scan size, 600 nm; scan rate, 1 Hz; number of samples/line, 512; line direction, retrace; capture direction, down; scan angle, 90°; control gain, 5; amplitude set point, 1.0 nN; drive amplitude, 120 nm at 2 kHz; spring constant, 0.5 N/m; tip radius, 10 nm.

spore core appeared to be soft and wet, while the cortex appeared to be stiff and dry. The coat of the spore appeared to have moderate stiffness and wetness. The outer layer of the cortex showed slightly lower adhesion and greater stiffness than the inner cortex layer (Fig. 6 and 7). It is worth mentioning that the relative orders of the nanomechanical properties for the spore core, cortex, and coat were consistent among all samples we studied. The dehydration state, measured by adhesion force, of the spore section showed few changes after the freshly created section was exposed to air for several days under ambient conditions, indicating good stability of the spore core against water uptake in air.

Thermal effects on the nanomechanical properties of the spore section. Figure 9 shows AFM deformation images of the spore section at elevated temperatures. The inner germ cell wall and outer cortex exhibited different thermal responses. At low temperatures below 195°C, there were two boundaries that were clearly visible (Fig. 9a, white and blue arrows). One belonged to the core-cortex interface (white arrow), and the other was the cortex-coat interface (blue arrow). However, when the temperature was increased to 230°C, the interface between the inner and outer cortex layer became apparent (Fig. 9b). The newly created boundary broadened and blurred at about 300°C. This result clearly indicated that the chemical composition at the interface between the germ cell wall and the cortex was significantly different from the nearby inner and outer cortex PG materials. The adhesion of the inner cortex layer increased sig-

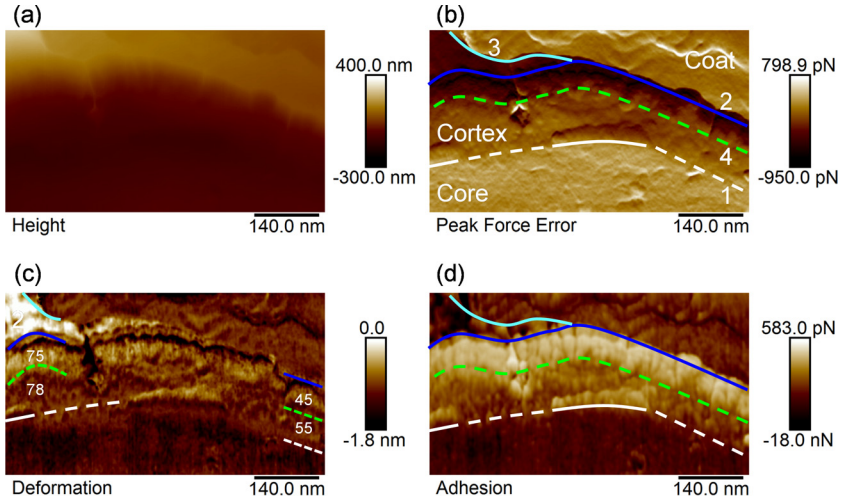

FIG 7 High-resolution AFM images (inverted) of the multilayer structure of the core, cortex, and coat of the spore at ambient temperature in air. (a) Height (rescaled). (b) Peak force. (c) Deformation. (d) Adhesion. The interface between the core and cortex is indicated by line 1. The well-defined boundaries are highlighted by the solid line, while the less well-defined boundaries are highlighted by the dotted lines. The interface between the cortex and coat is indicated by line 2. The boundary between the torn-off coat and air is labeled by line 3. The interface between two cortex layers is suggested by line 4.

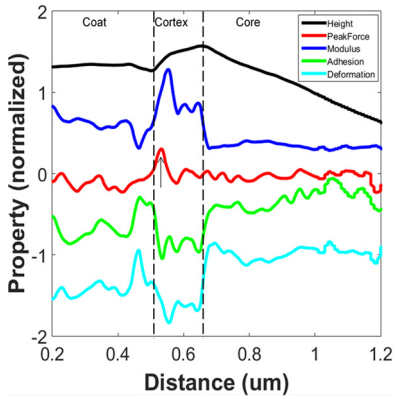

FIG 8 Changes of surface morphology and properties across the cross-section of a freshly cut spore (sample 1). All curves were normalized along the scan direction in the *x* axis and shifted in the *y* axis, except for the peak force curve. The modulus data were on the logarithmic scale. The following AFM parameters were used: scan size, 1,000 nm; scan rate, 1 Hz; number of samples/line, 512; line direction, retrace; capture direction, up; scan angle, 0°; control gain, 12; amplitude set point, 1.8 nN; drive amplitude, 120 nm at 2 kHz; spring constant, 0.5 N/m; tip radius, 10 nm.

nificantly at high temperatures (see Fig. S7 in the supplemental material).

More detailed results of thermal effects on spore section are shown in Fig. 10. The data we display in Fig. 10 were obtained from the selected area of the spore section, as highlighted by the rectangular dotted line in Fig. 3c. The raw modulus data were corrected based upon the coat modulus we measured previously (51). The mean modulus of the spore core showed no significant changes until the sample was heated at about 230°C. The core modulus increased slightly from about 1.2 to 1.6 GPa when the tip temperature was varied between 265 and 335°C. When the spore was cooled back to 20°C, the modulus decreased to about 0.9 GPa. The modulus of the coat and cortex decreased gradually by about 30% with increasing temperature from 20 to 230°C and remained nearly constant at about 2 GPa during the subsequent heating at higher temperatures. The mean adhesion of the spore core showed a small decrease from 13 to 10 nN as the tip temperature was increased from 20 to 230°C. The core adhesion reduced to less than 2 nN at temperatures between 265 and 335°C and increased quickly to about 33 nN after the spore was cooled down to 20°C. The temperature dependence of the modulus and adhesion for the coat and cortex showed a similar trend. The mean adhesion of the spore coat decreased from 7.8 to 5.8 nN as the tip temperature was increased from 20 to 230°C. The coat adhesion further reduced to less than 2 nN at temperatures between 265 and 335°C and increased slightly to about 2.5 nN after the spore was cooled down to 20°C. Similarly, the mean adhesion of the spore cortex decreased from 4.1 to 3.4 nN as the tip temperature was increased from 20 to 230°C. The cortex adhesion further reduced to less than 2 nN at temperatures between 265 and 335°C and increased slightly to about 2.5 nN after the spore was cooled down to 20°C. The statistical analysis indicates that the temperature dependence of the nanomechanical properties for the core, cortex, and coat were significant.

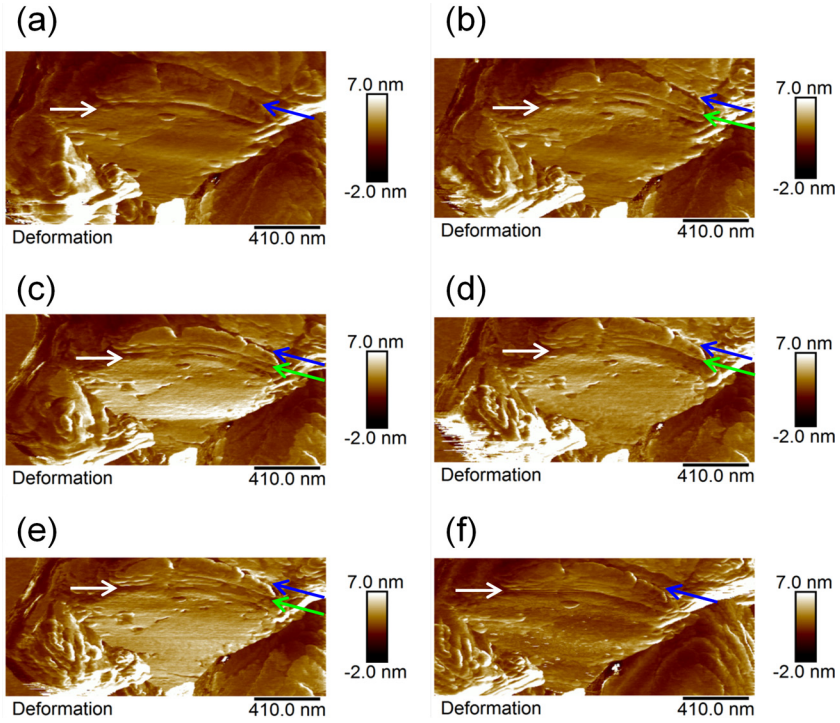

FIG 9 AFM deformation images of the cross-section of an air-dried *Bacillus anthracis* spore at elevated temperatures of 195°C (a), 230°C (b), 265°C (c), 300°C (d), 335°C (e), and 20°C (f) after cooling from 335°C in air. The interface between the core and cortex is indicated by the white arrow. The interface between the cortex and coat is indicated by the blue arrow. The interface between the germ cell wall (e.g., inner cortex) and outer cortex is indicated by the green arrow. The following AFM parameters were used: scan size, 2.1 μm; scan rate, 1 Hz; number of samples/line, 512; line direction, retrace; scan angle, 90°; control gain, 18; amplitude set point, 11.5 nN; drive amplitude, 120 nm at 2 kHz; spring constant, 2.5 N/m; tip radius, 30 nm.

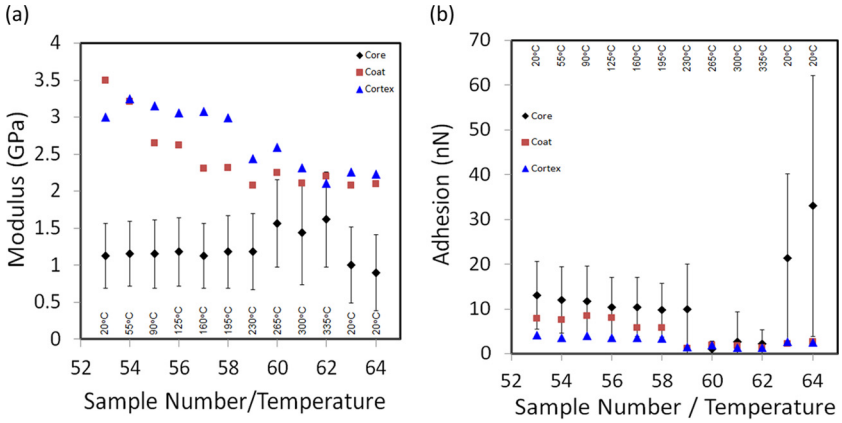

FIG 10 Influence of heat on the nanomechanical properties of the spore section, including the core, cortex, and coat. The spore section was imaged at elevated temperatures from 20 to 55, 90, 125, 160, 195, 230, 265, 300, and 335°C using the heated AFM tip before it was cooled to 20°C in air. The average dwelling time at each contact point is about 0.5 ms, corresponding to about 8 min for a whole-image scan. The modulus error bars for the coat and cortex (not shown) were comparable with those for the core. The adhesion error bars for the coat and the cortex (not shown) were significantly smaller than those for the spore core. The following AFM parameters were used: scan size, 2.1 μm; scan rate, 1 Hz; number of samples/line, 512; line direction, retrace; capture direction, down; scan angle, 0°; control gain, 18; amplitude set point, 11.5 nN; drive amplitude, 120 nm at 2 kHz; spring constant, 2.5 N/m; tip radius, 30 nm.

The low modulus of the core can be attributed to small DPA molecules and high water content in the spore core (24–27). The large modulus of the cortex can be related to the large, cross-linking PG polymers (31–41). The modulus of the proteinaceous coat appeared to be similar to that of the cortex PG polymers (42–44). It is clear that the cortex material was the more hydrophobic, while the core was the more hydrophilic structure in the spore section. These results appear to be consistent with the current hypothesis that spore water is trapped largely in the core by the DPA polymer network; the cortex maintains the state of dehydration of the spore by providing a hydrophobic layer that can hinder water diffusion in or out of the core. It should be pointed out that the spore core showed significant mechanical stability at elevated temperatures. For example, when the core was heated from 20 to 230°C, its modulus showed few changes, even though its adhesion force decreased by 23%. This may not come as a surprise, since the elastic modulus of a polymer is determined largely by its backbone structure. The adhesion force may be sensitive to changes in the arrangement of its size polar groups. The temperature at which the modulus showed a large increase and the adhesion showed a large decrease was slightly above the melting point of DPA (about 250°C), suggesting that the changes in the nanomechanical properties are associated with a phase transition of DPA in the spore core. The lack of periodic structures in the spore core indicated that it is in a glassy state. The large increase in the adhesion of the heated spore core, together with a small drop in the modulus, may signal irreversible thermal denaturation of the core materials. The spore structures appear to be able to withstand transient heating at temperatures of more than a hundred degrees higher than the temperature (e.g., about 150°C) that is routinely used to kill bacteria in most static heating environments.

Conclusions. We performed an AFM study on the surface morphology and nanomechanical properties of a cross-section of individual spores. The internal spore structures, such as the core and cortex, were exposed to a probing AFM tip by means of nanoindentation cutting with a diamond AFM tip. We observed that the nanomechanical properties, such as the adhesion and modulus, differed significantly in different regions of the spore cross-section. We found that the nanomechanical properties of the spore cross-section showed strong dependence upon the temperature. Our AFM images indicated that the PG cortex of *Bacillus anthracis* spores appeared to consist of rod-like nanometer-sized structures that are oriented perpendicular to the spore surface. Our findings may advance the understanding of spore architecture and properties.

ACKNOWLEDGMENT

The views expressed in this report are those of the authors and do not reflect the official position of the United States Air Force, Department of Defense, or U.S. Government.

FUNDING INFORMATION

This work, including the efforts of Alex Li, was partially funded by DOD | Defense Threat Reduction Agency (DTRA).

REFERENCES

1. **Tennen R, Setlow B, Davis KL, Loshon CA, Setlow P.** 2000. Mechanisms of killing of spores of Bacillus subtilis by iodine, glutaraldehyde and nitrous acid. J Appl Microbiol **89:**330–338. http://dx.doi.org/10.1046/j.1365-2672.2000.01114.x.
2. **Nicholson WL, Schuerger AC, Setlow P.** 2005. The solar UV environment and bacterial spore UV resistance: considerations for Earth-to-Mars transport by natural processes and human spaceflight. Mutat Res **571:** 249–264. http://dx.doi.org/10.1016/j.mrfmmm.2004.10.012.
3. **Nicholson WL, Munakata N, Horneck G, Melosh HJ, Setlow P.** 2000. Resistance of Bacillus endospores to extreme terrestrial and extraterrestrial environments. Microbiol Mol Biol Rev **64:**548–572. http://dx.doi.org/10.1128/MMBR.64.3.548-572.2000.
4. **Gerhardt P, Marquis RE.** 1989. Spore thermoresistance mechanisms, p 43–63. *In* Smith I, Slepecky RA, Setlow P (ed), Regulation of prokaryotic development. American Society for Microbiology, Washington, DC.
5. **McDonnell G, Russell AD.** 1999. Antiseptics and resistance: activity, action and resistance. Clin Microbiol Rev **12:**147–179.
6. **Chapman GB, Hillier J.** 1953. Electron microscopy of ultra-thin sections of bacteria I. Cellular division in Bacillus cereus. J Bacteriol **66:**362–373.
7. **Kornberg A, Spudich JA, Nelson DL, Deutscher M.** 1968. Origin of

proteins in sporulation. Annu Rev Biochem **37:**51–78. http://dx.doi.org/10.1146/annurev.bi.37.070168.000411.
8. **Holt SC, Leadbetter ER.** 1969. Comparative ultrastructure of selected aerobic spore-forming bacteria: a freeze-etching study. Bacteriol Rev **33:**346–378.
9. **Beaman TC, Pankratz HS, Gerhardt P.** 1972. Ultrastructure of the exosporium and underlying inclusions in spores of Bacillus megaterium strains. J Bacteriol **109:**1198–1209.
10. **Aronson AI, Fitz-James P.** 1976. Structure and morphogenesis of the bacterial spore coat. Bacteriol Rev **40:**360–402.
11. **Ebersold HR, Luthy P, Corier JL, Muller MA.** 1981. Freeze substitution and freeze-fracture study of bacterial spore structures. J Ultrastruct Res **76:**17–81.
12. **Graham LL, Beveridge TJ.** 1990. Effect of chemical fixatives on accurate preservation of Escherichia coli and Bacillus subtilis structure in cells prepared by freeze-substitution. J Bacteriol **172:**2150–2159.
13. **Graham LL, Beveridge TJ.** 1994. Structural differentiation of the Bacillus subtilis 168 cell wall. J Bacteriol **176:**1413–1421.
14. **Leuschner RG, Lillford PJ.** 2001. Investigation of bacterial spore structure by high resolution solid-state nuclear magnetic resonance spectroscopy and transmission electron microscopy. Int J Food Microbiol **63:**35–50. http://dx.doi.org/10.1016/S0168-1605(00)00396-2.
15. **Tocheva EI, López-Garrido J, Hughes HV, Fredlund J, Kuru E, Van Nieuwenhze MS, Brun YV, Pogliano K, Jensen GJ.** 2013. Peptidoglycan transformations during Bacillus subtilis sporulation. Mol Microbiol **88:**673–686. http://dx.doi.org/10.1111/mmi.12201.
16. **Tocheva EI, Matson EG, Morris DM, Moussavi F, Leadbetter JR, Jensen GJ.** 2011. Peptidoglycan remodeling and conversion of an inner membrane into an outer membrane during sporulation. Cell **146:**799–812. http://dx.doi.org/10.1016/j.cell.2011.07.029.
17. **Hachisuka Y, Kojima K, Sata T.** 1966. Fine filaments on the outside of the exosporium of Bacillus anthracis spores. J Bacteriol **91:**2382–2384.
18. **Popham DL.** 2013. Visualizing the production and arrangement of peptidoglycan in Gram-positive cells. Mol Microbiol **88:**645–649. http://dx.doi.org/10.1111/mmi.12212.
19. **Gan L, Chen SY, Jensen GJ.** 2008. Molecular organization of Gram-negative peptidoglycan. Proc Natl Acad Sci U S A **105:**18953–18957. http://dx.doi.org/10.1073/pnas.0808035105.
20. **Murrell WG.** 1969. Chemical composition of spores and spore structure, p 215–273. *In* Gould GW, Hurst A (ed), The bacterial spore. Academic Press, London, United Kingdom.
21. **Piggot P, Coote J.** 1976. Genetic aspects of bacterial endospore formation. Bacteriol Rev **40:**908–962.
22. **Warth A, Ohye D, Murrell W.** 1963. The composition and structure of bacterial spores. J Cell Biol **16:**579–592. http://dx.doi.org/10.1083/jcb.16.3.579.
23. **Henriques A, Moran CP, Jr.** 2000. Structure and assembly of the bacterial endospore coat. Methods **20:**95–110. http://dx.doi.org/10.1006/meth.1999.0909.
24. **Leanz G, Gilvarg C.** 1973. Dipicolinic acid location in intact spores of Bacillus megaterium. J Bacteriol **114:**455–456.
25. **Kozuka S, Yasuda Y, Tochikubo K.** 1985. Ultrastructural localization of dipicolinic acid in dormant spores of Bacillus subtilis by immunoelectron microscopy with colloidal gold particles. J Bacteriol **162:**1250–1254.
26. **Matano Y, Yasuda Y, Tochikubo K.** 1993. Evidence that dipicolinic acid is covalently bound to specific macromolecules in spores of Bacillus subtilis. FEMS Microbiol Lett **109:**189–194. http://dx.doi.org/10.1111/j.1574-6968.1993.tb06166.x.
27. **Lindsay JA, Murrell WG.** 1986. Solution spectroscopy of dipicolinic acid interaction with nucleic acids: role in spore heat resistance. Curr Microbiol **13:**255–259. http://dx.doi.org/10.1007/BF01568649.
28. **Setlow P.** 1988. Small, acid-soluble spore proteins of Bacillus species: structure, synthesis, genetics, function, and degradation. Annu Rev Microbiol **42:**319–338. http://dx.doi.org/10.1146/annurev.mi.42.100188.001535.
29. **Setlow P.** 1992. DNA in dormant spores of Bacillus species is in an A-like conformation. Mol Microbiol **6:**563–567. http://dx.doi.org/10.1111/j.1365-2958.1992.tb01501.x.
30. **Setlow B, Atluri S, Kitchel R, Koziol-Dube K, Setlow P.** 2006. Role of dipicolinic acid in resistance and stability of spores of Bacillus subtilis with or without DNA-protective α/β-type small acid-soluble proteins. J Bacteriol **188:**3740–3747. http://dx.doi.org/10.1128/JB.00212-06.
31. **Popham D.** 2002. Specialized peptidoglycan of the bacterial endospore. Cell Mol Life Sci **59:**426–433. http://dx.doi.org/10.1007/s000018-002-8435-5.
32. **Foster SJ, Johnstone K.** 1986. The use of inhibitors to identify early events during Bacillus megaterium KM spore germination. Biochem J **237:**865–870. http://dx.doi.org/10.1042/bj2370865.
33. **Thwaites JJ, Mendelson NH.** 1991. Mechanical behaviour of bacterial cell walls. Adv Microb Physiol **32:**173–222. http://dx.doi.org/10.1016/S0065-2911(08)60008-9.
34. **Typas A, Banzhaf M, Gross CA, Vollmer W.** 2012. From the regulation of peptidoglycan synthesis to bacterial growth and morphology. Nat Rev Microbiol **10:**123–136. http://dx.doi.org/10.1038/nrmicro2677.
35. **Verwer RW, Nanninga N.** 1976. Electron microscopy of isolated cell walls of Bacillus subtilis var. niger. Arch Microbiol **109:**195–197. http://dx.doi.org/10.1007/BF00425135.
36. **Santo LY, Doi RH.** 1974. Ultrastructural analysis during germination and outgrowth of Bacillus subtilis spores. J Bacteriol **120:**475–481.
37. **Popham DL, Helin J, Costello CE, Setlow P.** 1996. Muramic lactam in peptidoglycan of Bacillus subtilis spores is required for spore outgrowth but not for spore dehydration or heat resistance. Proc Natl Acad Sci U S A **93:**15405–15410. http://dx.doi.org/10.1073/pnas.93.26.15405.
38. **Thomas RS.** 1964. Ultrastructural location of mineral matter in bacterial spores by microincineration. J Cell Biol **23:**113–133. http://dx.doi.org/10.1083/jcb.23.1.113.
39. **Dmitriev BA, Toukach FV, Schaper KJ, Holst O, Rietschel ET, Ehlers S.** 2003. Tertiary structure of bacterial murein: the scaffold model. J Bacteriol **185:**3458–3468. http://dx.doi.org/10.1128/JB.185.11.3458-3468.2003.
40. **Dmitriev BA, Toukach FV, Holst O, Rietschel ET, Ehlers S.** 2004. Tertiary structure of Staphylococcus aureus cell wall murein. J Bacteriol **186:**7141–7148. http://dx.doi.org/10.1128/JB.186.21.7141-7148.2004.
41. **Hayhurst EJ, Kailas L, Hobbs JK, Foster SJ.** 2008. Cell wall peptidoglycan architecture in Bacillus subtilis. Proc Natl Acad Sci U S A **105:**14603–14608. http://dx.doi.org/10.1073/pnas.0804138105.
42. **McKenney PT, Eichenberger P.** 2012. Dynamics of spore coat morphogenesis in Bacillus subtilis. Mol Microbiol **83:**245–260. http://dx.doi.org/10.1111/j.1365-2958.2011.07936.x.
43. **Driks A.** 2002. Maximum shields: the assembly and function of the bacterial spore coat. Trends Microbiol **10:**251–254. http://dx.doi.org/10.1016/S0966-842X(02)02373-9.
44. **Driks A.** 1999. Bacillus subtilis spore coat. Microbiol Mol Biol Rev **63:**1–20.
45. **Westphal AJ, Price PB, Leighton TJ, Wheeler KE.** 2003. Kinetics of size changes of individual Bacillus thuringiensis spores in response to changes in relative humidity. Proc Natl Acad Sci U S A **100:**3461–3466. http://dx.doi.org/10.1073/pnas.232710999.
46. **Sahin O, Yong EH, Driks A, Mahadevan L.** 2012. Physical basis for the adaptive flexibility of Bacillus spores. J R Soc Interface **9:**3156–3160. http://dx.doi.org/10.1098/rsif.2012.0470.
47. **Plomp M, Leighton TJ, Wheeler KE, Hill HD, Malkin AJ.** 2007. In vitro high-resolution structural dynamics of single germinating bacterial spores. Proc Natl Acad Sci U S A **104:**9644–9649. http://dx.doi.org/10.1073/pnas.0610626104.
48. **Plomp M, Carroll AM, Setlow P, Malkin AJ.** 2014. Architecture and assembly of the Bacillus subtilis spore coat. PLoS One **9:**e108560. http://dx.doi.org/10.1371/journal.pone.0108560.
49. **Plomp M, Leighton TJ, Wheeler KE, Malkin AJ.** 2005. Architecture and high-resolution structure of Bacillus thuringiensis and Bacillus cereus spore coat surfaces. Langmuir **21:**7892–7898. http://dx.doi.org/10.1021/la050412r.
50. **Plomp M, McCaffery JM, Cheong I, Huang X, Bettegowda C, Kinzler KW, Zhou S, Vogelstein B, Malkin AJ.** 2007. Spore coat architecture of Clostridium novyi NT spores. J Bacteriol **189:**6457–6468. http://dx.doi.org/10.1128/JB.00757-07.
51. **Chada VGR, Sanstad EA, Wang R, Driks A.** 2003. Morphogenesis of Bacillus spore surfaces. J Bacteriol **185:**6255–6261. http://dx.doi.org/10.1128/JB.185.21.6255-6261.2003.
52. **Giorno R, Bozue J, Cote C, Wenzel T, Moody KS, Mallozzi M, Ryan M, Wang R, Zielke R, Maddock JR.** 2007. Morphogenesis of the Bacillus anthracis spore. J Bacteriol **189:**691–705. http://dx.doi.org/10.1128/JB.00921-06.
53. **Wang R, Krishnamurthy SN, Jeong JS, Driks A, Mehta M, Gingras BA.** 2007. Fingerprinting species and strains of Bacilli spores by distinctive coat surface morphology. Langmuir **23:**1023–1024.
54. **Zolock RA, Li G, Bleckmann C, Burggraf LW, Fuller DC.** 2006.

Atomic force microscopy of Bacillus spore surface morphology. Micron **27:**36–39.
55. **Li AG, Xing Y, Burggraf LW.** 2013. Thermal effects on surface structures and properties of Bacillus anthracis spores on nanometer scales. Langmuir **29:**8343–8354. http://dx.doi.org/10.1021/la400992q.
56. **Xing Y, Li GA, Felker DL, Burggraf LW.** 2014. Nanoscale structural and mechanical analysis of Bacillus anthracis spores inactivated with rapid dry heating. Appl Environ Microbiol **80:**1739–1749. http://dx.doi.org/10.1128/AEM.03483-13.
57. **Bradbury JH, Foster JR, Hammer B, Lindsay J, Murrell WG.** 1981. The source of the heat resistance of bacterial spores: study of water in spores by NMR. Biochim Biophys Acta **678:**157–164. http://dx.doi.org/10.1016/0304-4165(81)90201-4.
58. **Ghosal S, Leighton TJ, Wheeler KE, Hutcheon ID, Weber PK.** 2010. Spatially resolved characterization of water and ion incorporation in Bacillus spores. Appl Environ Microbiol **76:**3275–3282. http://dx.doi.org/10.1128/AEM.02485-09.
59. **Bowden N, Brittain S, Evans AG, Hutchinson JW, Whitesides GM.** 1998. Spontaneous formation of ordered structures in thin films of metals supported on an elastomeric polymer. Nature **393:**146–149. http://dx.doi.org/10.1038/30193.
60. **Maugis D.** 2000. Contact, adhesion and rupture of elastic solids, p 203–344. Springer-Verlag, Berlin, Germany.
61. **Hutter JL, Bechhoefer J.** 1993. Calibration of atomic force microscope tips. Rev Sci Instrum **64:**1868–1873. http://dx.doi.org/10.1063/1.1143970.
62. **Li AG, Burggraf LW.** 2010. Glass transitions in nanoscale heated volumes of thin polystyrene films. Rev Sci Instrum **81:**123707–123711. http://dx.doi.org/10.1063/1.3529016.